coatings

Article

Solution and Double Aging Treatments of Cold Sprayed Inconel 718 Coatings

Wen Sun [1,2,*], Xin Chu [1,2], Jibo Huang [1], Haiming Lan [1], Adrian Wei-Yee Tan [3], Renzhong Huang [1] and Erjia Liu [4]

[1] National Engineering Laboratory for Modern Materials Surface Engineering Technology, Institute of New Materials, Guangdong Academy of Sciences, Guangzhou 510650, China; chuxin@gdinm.com (X.C.); huangjibo@gdinm.com (J.H.); lanhaiming@gdinm.com (H.L.); huangrenzhong@gdinm.com (R.H.)
[2] School of Materials Science and Engineering, South China University of Technology, Guangzhou 510641, China
[3] School of Engineering, University of Southampton Malaysia, Iskandar Puteri 79200, Malaysia; adrian.tan@soton.ac.uk
[4] School of Mechanical and Aerospace Engineering, Nanyang Technological University, 50 Nanyang Avenue, Singapore 639798, Singapore; mejliu@ntu.edu.sg
* Correspondence: sunw0013@e.ntu.edu.sg

Abstract: In this study, Inconel 718 coatings were deposited by the high-pressure cold spray technique, and post-process solution and double aging treatments were conducted. The microstructures of the as-deposited and heat-treated IN718 were analyzed, and their mechanical properties were tested. It was found that the micro-dendritic structures in the original powder were severely elongated in the as-deposited IN718 coating due to plastic deformation during the cold spray process. After solution heat treatment, Nb, Mo, and Ti-rich segregations could be dissolved, transforming to MC carbide and a needle-like δ phase. It was found that the needle-like δ phase at the grain boundary had a pinning effect to slow down the grain growth. In addition, strengthening phases could be formed by aging treatments. The mechanical properties of the cold sprayed Inconel 718 could be improved by proper solution and aging heat treatments.

Keywords: cold spray; Inconel 718; solution treatment; aging treatment; microstructure; mechanical properties

check for updates

Citation: Sun, W.; Chu, X.; Huang, J.; Lan, H.; Tan, A.W.-Y.; Huang, R.; Liu, E. Solution and Double Aging Treatments of Cold Sprayed Inconel 718 Coatings. *Coatings* **2022**, *12*, 347. https://doi.org/10.3390/coatings12030347

Academic Editor: Paolo Castaldo

Received: 31 December 2021
Accepted: 24 February 2022
Published: 7 March 2022

1. Introduction

Inconel 718 (hereafter 'IN718') is a precipitation-strengthened nickel-base superalloy mainly by nanoscale γ'' (Ni3Nb) and γ' (Ni3(Al, Ti)) phases in the γ matrix [1,2]. IN718 is extensively used in gas turbine disks, aircraft engines, rocket motors, and nuclear reactors due to its excellent mechanical properties and high fatigue life, creep resistance, and surface stability at elevated temperatures [3]. However, for those components made by nickel-based superalloys, damage in service does occasionally occur and brings significant losses in profitability and time [4]. Cold spray (CS) technology as a rapid solid-state additive manufacturing (AM) technique can provide an effective way to restore both geometrical and mechanical properties of these damaged components [5,6]. CSAM technology has drawn increasingly more attention in recent decades due to its unique characteristics, such as low heat input, extremely high strain rate deformation of particles, solid-state deposition, and favorable mechanical properties [7,8].

Our previous research work found that the as-sprayed IN718 coating comprises simply of the γ-grains and interestingly no strengthening intermetallic phases such as γ'', γ', and δ phases [4]. In addition, there is a strong segregation of Nb and Mo elements in the inner-dendrite area and it could make the material more brittle and easily fail. Thus, applying post-process heat treatments to CS IN718 coatings is necessary to enhance interparticle chemical diffusion and remove the compositional segregation to obtain a homogeneous microstructure, which has rarely been investigated by other researchers.

Wong et al. [9] studied the effect of annealing heat treatments (i.e., 950 °C/2 h, 1010 °C/2 h, 1060 °C /2 h, and 1250 °C/1 h) on microstructure evolutions and tensile strengths of the cold sprayed IN718 coatings. The results showed that interparticle metallurgical bonding could be enhanced by annealing heat treatment, resulting in a higher tensile strength and better ductility. Pérez-Andrade et al. [10] applied post-heat treatment procedures by hot isostatic pressing (i.e., 1163 ± 14 °C/4 h), thermal soft annealing (i.e., 538 ± 14 °C/1 h, followed by 954 ± 14 °C/1 h), and aging (i.e., 760 ± 14 °C/5 h, followed by 649 ± 14 °C/1 h) for cold sprayed IN718 coatings, and it was found that heat treatment caused precipitation hardening and reduced work hardening effects, and M23C6 carbides and the δ-phase were observed in the heat-treated IN718 samples. Levasseur et al. [11] applied pressureless sintering on cold sprayed IN718 coatings at temperatures of 1200 °C, 1225 °C, and 1250 °C for 10, 60, and 180 min, and it was found that the pressureless sintering could significantly improve the flexural strength and ductility of the cold sprayed Inconel 718 coatings, and the evolution of the grain size during sintering was strongly correlated to the precipitation of secondary carbides.

To the best of the authors' knowledge, there still lacks a systematic study reporting the effects of solution and aging on the microstructure evolutions and mechanical properties of cold sprayed IN718 coatings. In this study, a series of solution and double aging treatments were applied to cold sprayed IN718 coatings, and the corresponding microstructure evolutions and mechanical properties were systematically investigated.

2. Materials and Methods

Commercially available plasma-atomized IN718 powder (AP&C, Boisbriand, QC, Canada) (15–45 µm) was used to fabricate the cold sprayed IN718 coatings. The substrates used in this study were IN718 plates (AP&C, Boisbriand, QC, Canada). A high-pressure cold spray system was used to perform the coating deposition. Nitrogen was used as the propellant gas that was preheated to 1000 °C and 4.5 MPa [12–14]. Solution treatment was conducted at 900 °C, 950 °C, 1000 °C, and 1050 °C (designated as S900, S950, S1000, and S1050, respectively) for 1.5 h followed by water quenching, and then double aging (designated as DA) was conducted at 720 °C for 8 h and 620 °C for 8 h [15,16]. The schematic illustrations of the heat treatment cycles are shown in Figure 1.

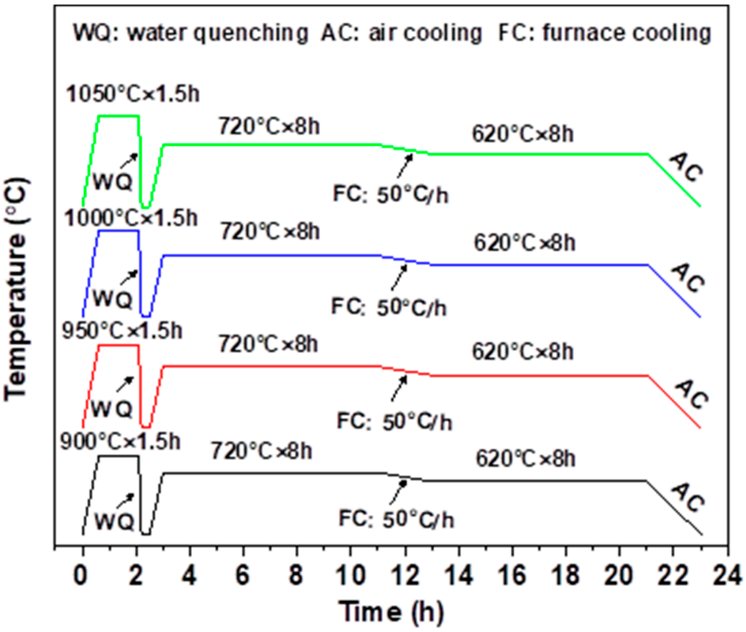

Figure 1. Schematic illustrations of the heat treatment cycles performed in this study.

The feedstock powders were characterized with field emission scanning electron microscopy (FESEM, JEOL, Tokyo, Japan) and electron backscatter diffraction (EBSD, Oxford, UK). The EBSD was taken by using a 0.2 µm step size. After cold spray deposition and heat treatment, the coating microstructure was measured by using optical microscopy (Zeiss, Jena, Germany). Coating porosities were measured with the ImageJ software (Version 1.53). The cross-sectional microstructures of the coatings were analyzed by using FESEM and EBSD. Microhardness values were evaluated by using a Vickers hardness tester (Future-Tech, Kanagawa, Japan) under a load of 500 gf. The dimensions of the tensile specimens of the freestanding IN718 coatings are shown in Figure 2. The tensile tests were carried out with an Instron testing machine (Zwick Roell Group, Ulm, Germany) with an extension rate of 0.4 mm/min.

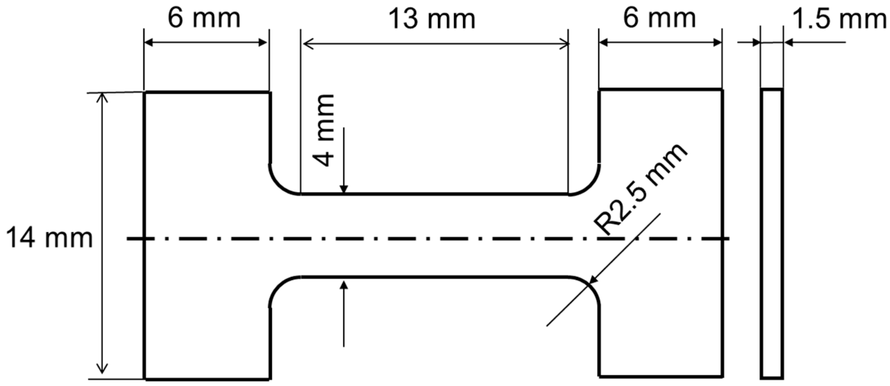

Figure 2. Dimensions of the tensile samples of the IN718 coatings.

3. Results and Discussions

3.1. Powder Characterization

Figure 3a shows the SEM micrograph of the IN718 powder and the inset is an enlarged view of most of the particles falling within the size range of 20–45 µm, and the average particle size is 32 µm. Figure 3c shows the Inverse Pole Figure (IPF) micrograph of the IN718 particles obtained from EBSD. It is clear that the individual particles contain a number of randomly oriented equiaxed grains, while some small particles contain single grains. Figure 3d shows the grain size distribution in the IN718 particles. It can be seen that most grains are 1–4 µm and some large grains range from 10 µm to 25 µm within the particles.

Figure 4a shows the backscatter electron (BSE) image of the powder cross-section where no internal porosity can be observed. Micro-dendritic structures can be seen throughout the particle volume, which is caused by the solidification partition coefficient difference of the element compositions during the rapid solidification experienced by the powder in the plasma atomization process (the quenching rate experienced by molten metal as it solidifies is around 10^5 °C/s during the plasma atomization process [17]). Figure 4b shows an enlarged view of the 'red square' in Figure 4a, and Figure 4c shows the corresponding EDS mapping results of different chemical elements. It can be seen that Nb, Mo, and Ti are higher in the interdendritic spaces (white phase 2) than the primary dendrites (grey phase 1), which agrees well with the elemental mapping results obtained in previous work [18,19]. Meanwhile, Ni, Cr, and Fe are more prone to aggregating in the dendrite cores. The dendrite arm spacing (DAS) shown in Figure 3c is very fine (around 1–2 µm), compared to the typical DAS in cast IN718 microstructures (10 µm–40 µm) [20], which can be attributed to the rapid cooling rate during the plasma atomization process. It was also reported by Mostafa et al. [18] that the white phase in the interdendritic space regions was recognized as a γ''-phase (bct-Ni3Nb) and the grey phase in primary dendrites was a γ-phase (Ni-Cr solid solution). However, it was also reported that the Nb- and Mo-rich intermetallic compound in the interdendritic area is a Laves phase [21]. Table 1 shows the chemical compositions of the primary dendrite and interdendritic phase in IN718 powder.

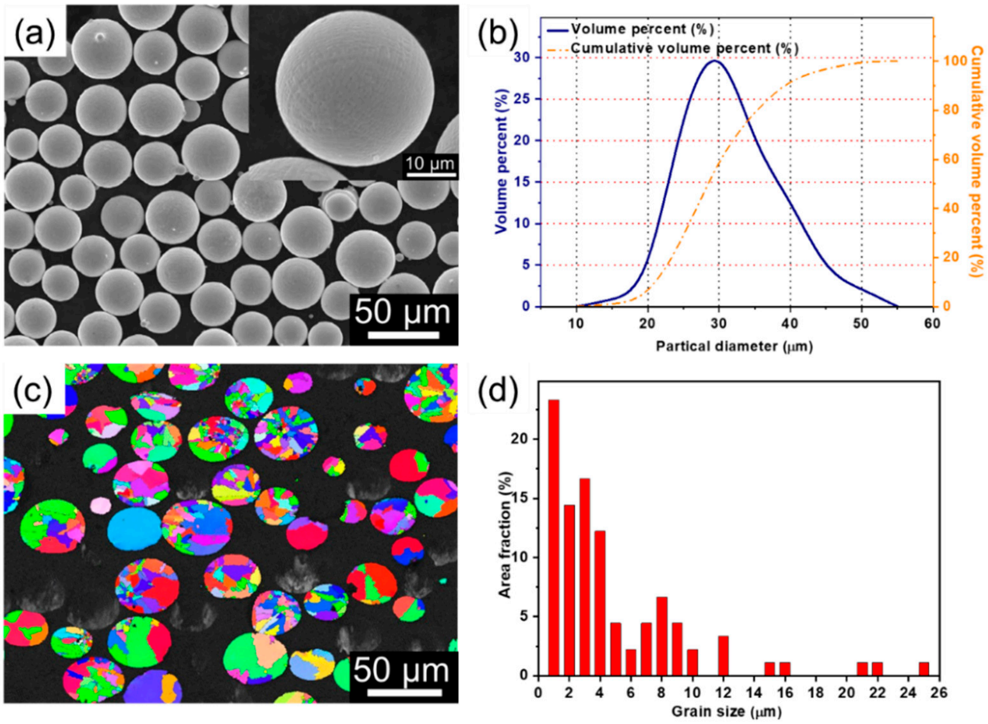

Figure 3. (**a**) SEM micrographs of IN718 powder feedstock in different magnifications, (**b**) particle size distribution, (**c**) inverse pole figure map of as-received IN718 powder, and (**d**) grain size distribution in as-received IN718 powder.

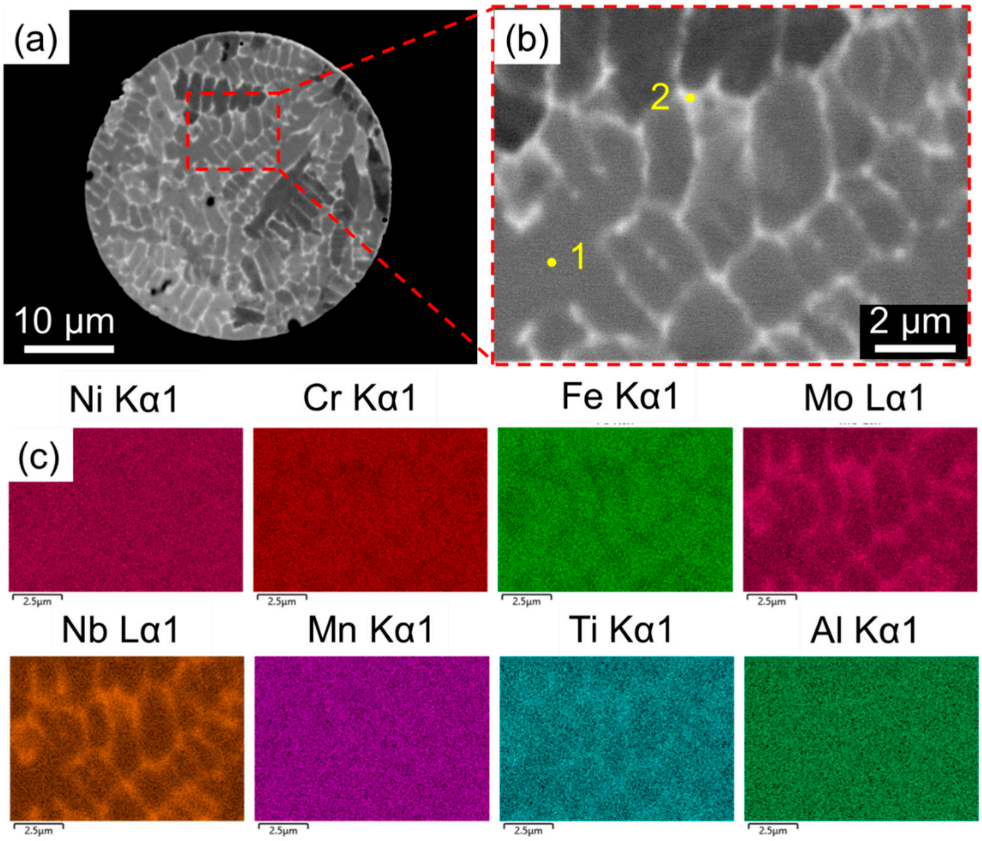

Figure 4. (**a**) BSE-SEM cross-sectional micrograph of an IN718 particle, (**b**) an enlarged view of the 'red square' in (**a**), and (**c**) the corresponding EDS mappings of different chemical elements.

Table 1. Chemical compositions of primary dendrite and interdendritic phase in IN718 powder.

Spots	Phases	Compositions (wt.%)							
		Ni	Cr	Fe	Mo	Nb	Mn	Ti	Al
1	Primary dendrite	53.4	20.3	20.6	2.5	2.0	0.1	0.5	0.5
2	Interdendritic phase	48.9	17.3	15.4	3.9	12.3	0.1	1.6	0.5

3.2. Microstructure Characterization

Figure 5 shows the optical micrographs and porosity levels of the as-sprayed and heat-treated IN718 coatings. In the as-sprayed coating, there is no obvious cracking observed within the coating. However, some irregular pores are present at the junctions of multiple neighboring splats due to insufficient deformation of the particles during the impact process, which are scattered throughout the coating. Porosity measurements were performed for the as-sprayed and heat-treated IN718 coatings by taking a series of images across the coating in a 10 mm × 10 mm area. From the 2D image analysis, the porosity level of the as-sprayed coating is around 1.7%. The micropores and weakly bonded particle boundaries within the as-sprayed coatings are regarded as defects, which can act as crack initiation points under external stress, thus causing a reduction in mechanical properties as compared to fully dense materials. After solution and double aging treatments, the coating porosity levels gradually reduce to around 1.32%, 1.29%, 1.13%, and 1.02% for S900 + DA, S950 + DA, S1000 + DA, and S1050 + DA samples, respectively, as shown in Figure 5b–e.

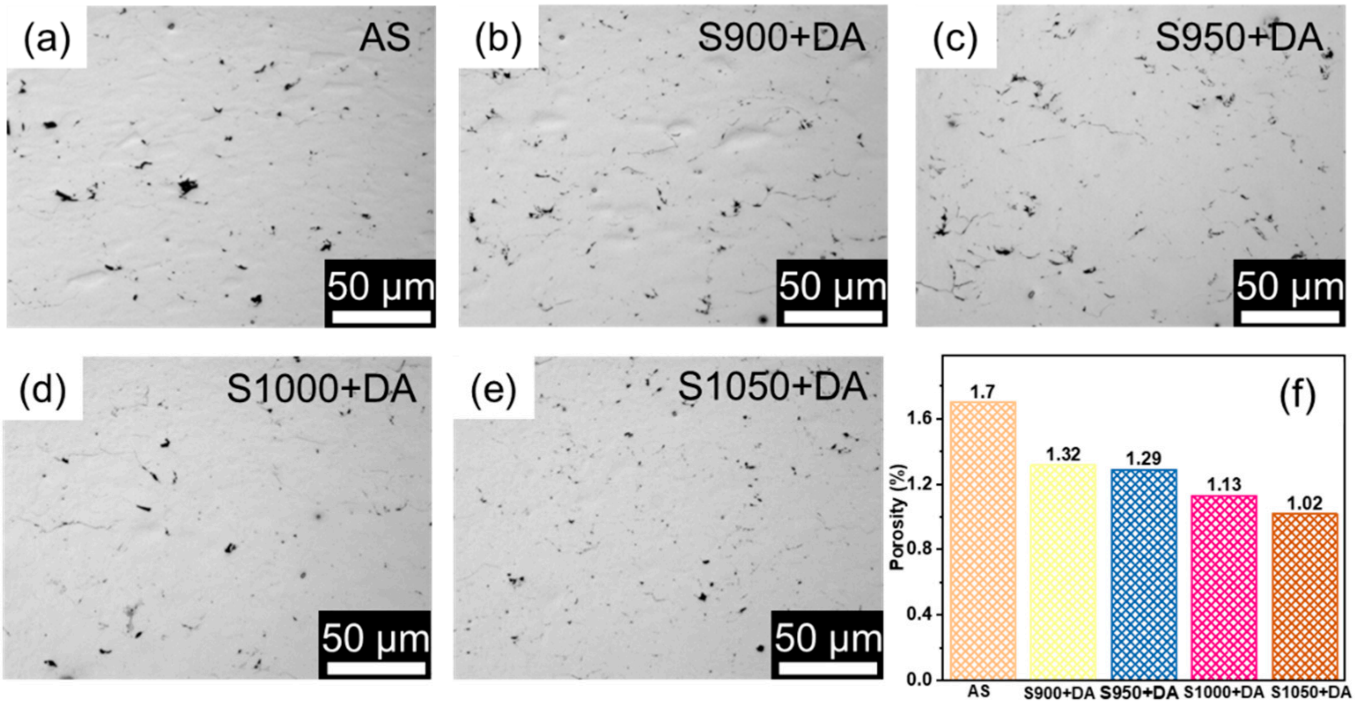

Figure 5. (**a**–**e**) Optical micrographs of cold sprayed IN718 coatings under different conditions: (**a**) as-sprayed, (**b**) S900 + DA, (**c**) S950 + DA, (**d**) S1000 + DA, and (**e**) S1050 + DA; (**f**) porosity levels of as-sprayed and heat-treated IN718 coatings.

Figure 6a–e show the cross-sectional BSE-SEM images of the as-sprayed and heat-treated IN718 coatings. In the as-sprayed state, as shown in Figure 6a,a′, it can be seen that a large degree of plastic deformation for the splats and severe elongation of the dendritic structures occur during cold spray deposition, which is caused by the high kinetic energy of the sprayed particles upon impact. After solution treatments, considerable heavy element segregations within the interdendritic regions dissolve into the γ matrix.

In addition, dendritic structures transform to equiaxed grains after heat treatment due to the recrystallization occurring during the heat treatment process. In addition to this, there are new precipitations formed after heat treatment. Figure 6b,b′ shows the BSE-SEM images of the S900 + DA sample where small white precipitates are present at grain boundaries. The EDS results show that these blocky precipitates have high Nb and Ti concentrations compared to the matrix, which can be identified as secondary MC carbides (M = Nb, Ti) [11]. The carbides mainly precipitated at grain boundaries but could also be found in the grain interiors. The short-rod and needle-like phase formed at grain boundaries can be identified as a δ phase. Previously observed precipitates with similar morphologies, compositions, and locations in heat-treated IN718 alloys were also confirmed as a δ phase [22–25]. Figure 6c,c′ shows the BSE-SEM images of the S950 + DA sample. Figure 7 shows an SEM micrograph of S950 + DA sample and the EDS results of the various phases. It can be seen that fewer white precipitates are present in the sample compared with the S900 + DA sample, because the δ-phase dissolves into the γ matrix. Another microstructure feature for the S950 + DA sample is that the grains grow larger due to the higher solution temperature, as well as the decreased numbers of δ-phase precipitates at the grain boundaries, thus decreasing the Zener pinning effect. With the solution temperature further increasing, the number of precipitates further decreases, and there are almost no precipitates observed in the sample after S1050 + DA treatments because the 1050 °C exceeds the solvus of δ phase [26]. The γ' phase and γ'' phase usually precipitate between 600 °C and 900 °C, which uniformly distribute in the γ matrix. These strengthening phases should be precipitated by double aging heat treatment, but they could not be statistically analyzed in the SEM micrograph, because the sizes of the γ' and γ'' phases are very small. γ'' phases are round-shaped and about 20 nm in size [27].

EBSD mapping was performed across the length of the heat-treated IN718 coatings, covering an area at the center of the coatings, as shown in Figure 8. For the S900 + DA sample, the grain size ranges from 0.9 μm to 9.5 μm, with an average grain size of 2.1 μm. It can be seen that the microstructure is not uniform, as a result of the inhomogeneous deposition process, as shown by the mixture of fine grains in the region of particle/particle boundaries and some larger grains in the central regions of the particles [28,29]. For the S950 + DA sample, the grain size ranges from 1.1 μm to 10.9 μm, with an average grain size of 2.4 μm. For the S1000 + DA sample, the grain size ranges from 1.8 μm to 19.4 μm, with an average grain size of 4.4 μm. For the S1050 + DA sample, the grain size ranges from 1.8 μm to 34.6 μm, with an average grain size of 5.5 μm. It can be seen that the grain structures become coarser with the solution temperature. The heat input leads to epitaxial growth of the grains. In addition, the microstructure of the S1050 + DA sample, unlike the other samples, displays a very high proportion of annealing twin boundaries.

3.3. Mechanical Properties

The results of microhardness testing of the IN718 samples are shown in Figure 9a. Under the as-sprayed condition, the IN718 deposit shows a hardness of around 470 HV0.3, which is much higher than that of the soft-annealed IN718 substrate with a hardness of around 240 HV0.3. The high hardness of the as-sprayed coating is due to the combined effects of work hardening, the high-density dislocations induced, and grain refinement occurrence during the cold spray process. After solution and double aging treatments, all samples show a statistically similar hardness of about 440 HV0.3. The coating hardness values slightly drop compared to those of the as-sprayed coating, which can be attributed to residual stress relief and the decrease in the work hardening effect during solution and aging treatments. The differences between deposits after different treatments are due to the combined effects of different porosity levels, precipitation hardening, and recrystallization and grain sizes [30,31].

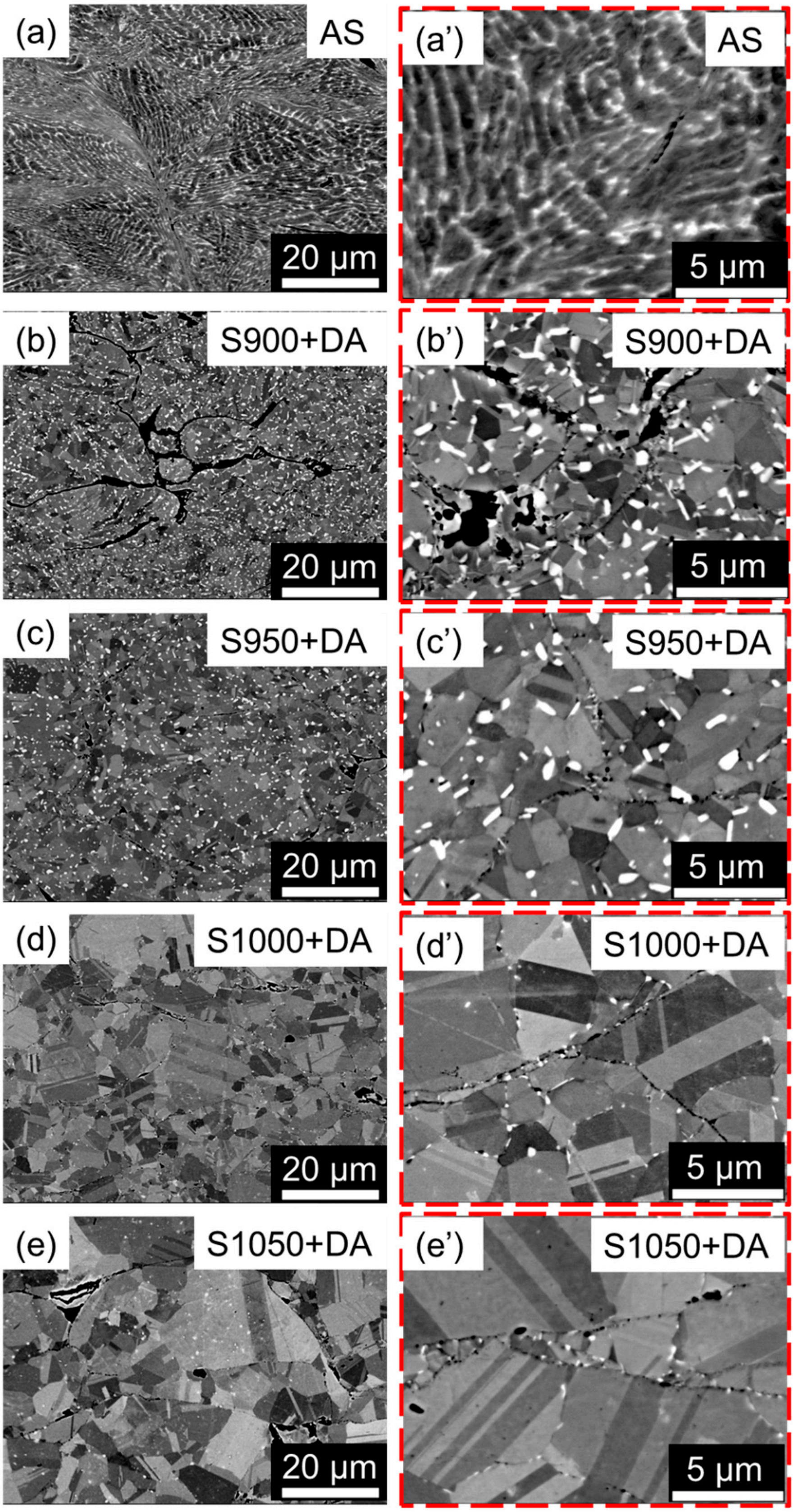

Figure 6. BSE-SEM micrographs of cold sprayed IN718 coatings under different conditions: (**a**,**a'**) as-sprayed, (**b**,**b'**) 900 °C solution + double aging, (**c**,**c'**) 950 °C solution + double aging, (**d**,**d'**) 1000 °C solution + double aging, and (**e**,**e'**) 1050 °C solution + double aging.

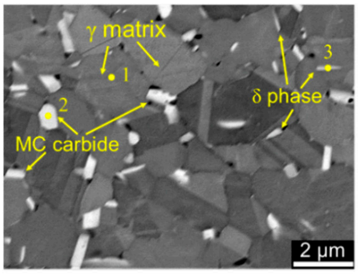

Spots	Phases	Composition(wt.%)							
		Ni	Cr	Fe	Mo	Nb	Mn	Ti	Al
1	γ matrix	52.4	20.0	19.6	3.1	3.5	0.1	0.8	0.5
2	MC carbide	59.0	10.8	7.7	2.0	18.2	0.1	2.0	0.1
3	δ phase	62.2	6.8	7.3	1.9	19.2	0.1	2.3	0.2

Figure 7. BSE SEM micrograph of S950 + DA sample showing a number of EDS point scans, and their respective chemical compositions of the various phases.

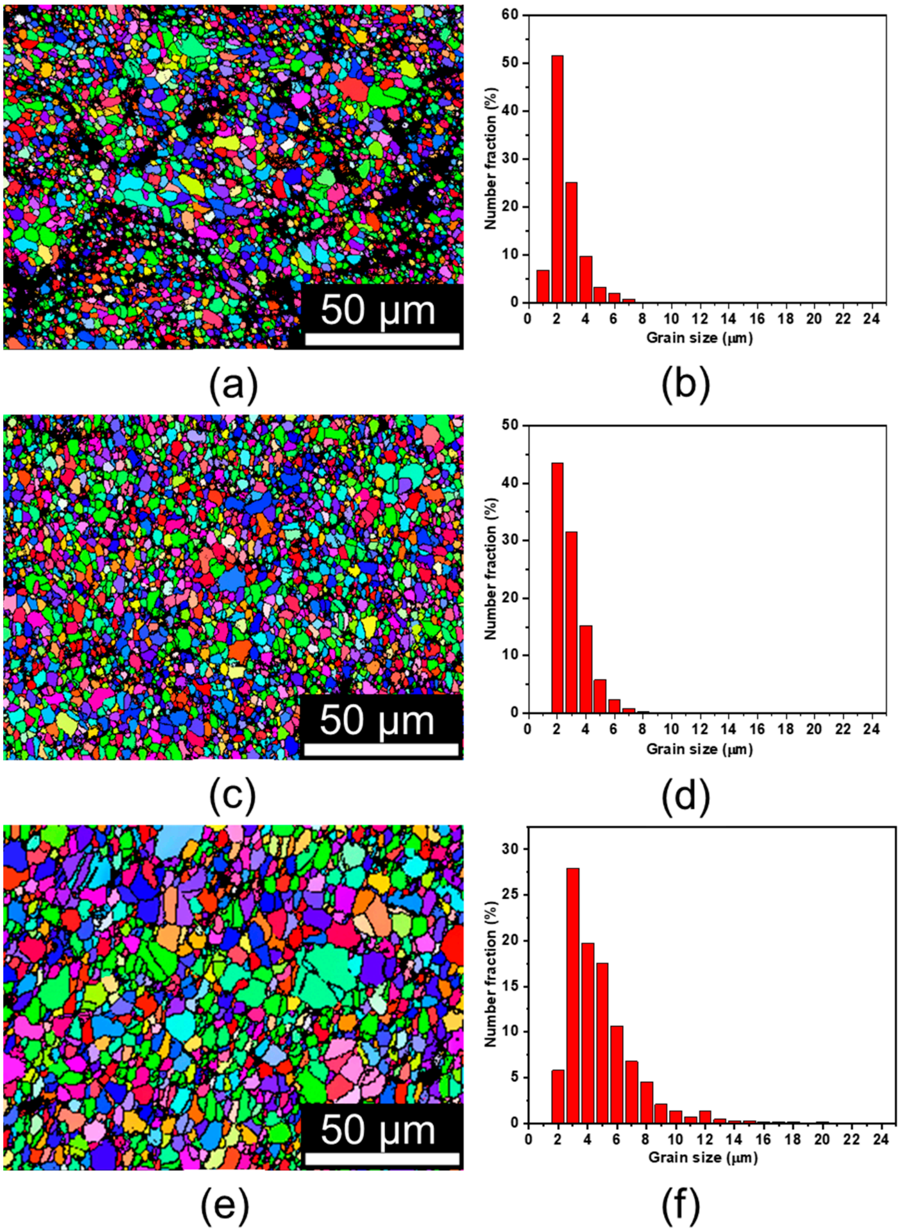

Figure 8. *Cont.*

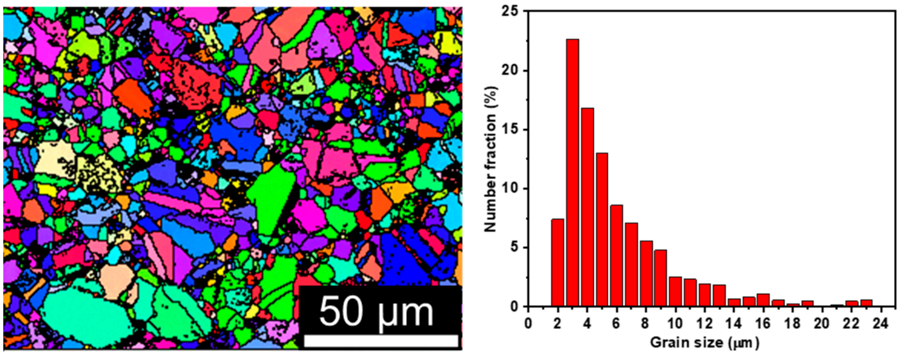

(g) (h)

Figure 8. (**a**–**d**) Inverse pole figure (IPF) maps and (**e**–**h**) grain size distributions of the CS IN718 coatings obtained by EBSD characterization under different conditions: (**a**,**e**) 900 °C solution + double aging, (**b**,**f**) 950 °C solution + double aging, (**c**,**g**) 1000 °C solution + double aging, and (**d**,**h**) 1050 °C solution + double aging.

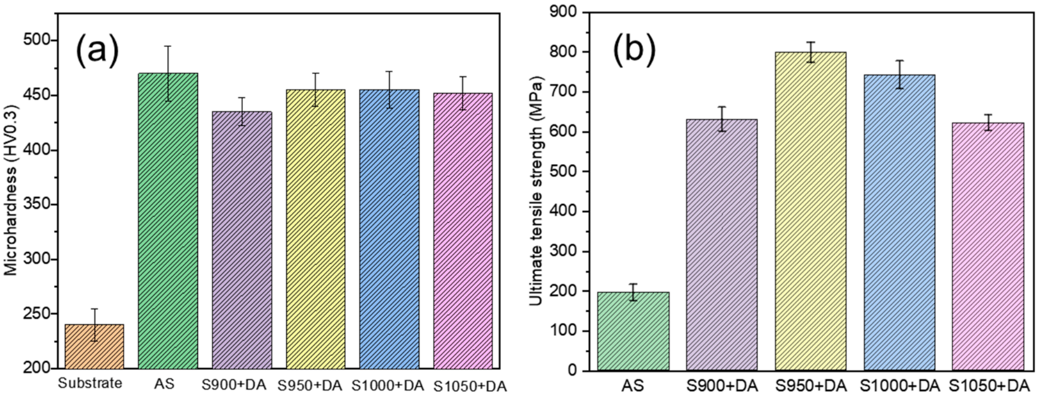

Figure 9. Vickers microhardness (**a**) and ultimate tensile strengths (**b**) of IN718 deposits in the as-sprayed and heat-treated conditions.

The tensile strength was measured on as-sprayed and heat-treated samples. Figure 9b shows the tensile strengths of the as-sprayed and heat-treated coatings. The tensile strength of the as-sprayed coating is around 196 MPa. The heat-treated coatings show a large increase in the ultimate tensile strength of approximately 2 to 3 times higher than that of the as-sprayed coating. Among all the heat-treated samples, the S950 + DA sample has the highest tensile strength of around 798 MPa, while the S1050 + DA sample has the lowest tensile strength of around 620 MPa, which can be attributed to multiple combined factors. First, heat treatments lead to enhanced diffusion at the particle boundaries, which could significantly improve the ultimate tensile strength of the IN718 samples. Secondly, the S950 + DA sample has smaller grain sizes compared to the S1000 + DA and S1050 + DA samples, which results in a higher ultimate tensile strength for the S950 + DA sample according to the Hall–Petch effect. Thirdly, the S950 + DA sample has less δ and MC carbide phases compared to the S900 + DA sample.

4. Conclusions

In this study, IN718 powder was successfully deposited by the cold spray process, and post-process solution and aging treatments were applied. The following conclusions have been drawn from our work:

(1) Solution and aging treatments could enhance diffusion among the deformed particles and lower the porosity level of the cold sprayed IN718, thus significantly improving the ultimate tensile strength.

(2) After solution and aging treatments, considerable heavy element segregations within the interdendritic regions dissolved into the γ matrix. The dendritic structures transformed to equiaxed grains caused by the recrystallization occurring during the heat treatment process.

(3) Carbides and δ-phase precipitates were present within the IN718 specimen after solution and aging treatments at 900 °C and 950 °C. When the solution temperature increased to 1000 °C, the quantities of the precipitations were significantly reduced, and the plate-like δ-phase transformed to a spheroidal δ phase. The grains grew coarser with the increase in solution temperature, and twin boundaries were present in the S1050 + DA samples.

(4) The tensile strength of the CS IN718 deposits were controlled by multiple combined factors. With proper solution and aging treatments, the mechanical properties of the heat-treated CS IN718 deposits could be comparable to the bulk IN718 fabricated by casting and forging.

Author Contributions: Conceptualization, W.S.; methodology, W.S.; formal analysis, W.S.; investigation, W.S.; resources, R.H. and E.L.; data curation, W.S.; writing—original draft preparation, W.S.; writing—review and editing, X.C., J.H., A.W.-Y.T., H.L. and E.L.; supervision, R.H. and E.L.; project administration, R.H. and W.S.; funding acquisition, R.H. and W.S. All authors have read and agreed to the published version of the manuscript.

Funding: Guangdong Academy of Sciences Special Fund for Comprehensive Industrial Technology Innovation Center Building (No. 2022GDASZH-2022010107); Key-Area Research and Development Program of Guangdong Province (No. 2020B0101330001); Science and Technology Program of Guangzhou (No. 202007020008).

Institutional Review Board Statement: Not applicable.

Informed Consent Statement: Not applicable.

Data Availability Statement: Not applicable.

Conflicts of Interest: The authors declare no conflict of interest.

References

1. Amato, K.N.; Gaytan, S.M.; Murr, L.E.; Martinez, E.; Shindo, P.; Hernandez, J.; Collins, S.; Medina, F. Microstructures and mechanical behavior of Inconel 718 fabricated by selective laser melting. *Acta Mater.* **2012**, *60*, 2229–2239. [CrossRef]
2. Sui, S.; Tan, H.; Chen, J.; Zhong, C.; Li, Z.; Fan, W.; Gasser, A.; Huang, W. The influence of Laves phases on the room temperature tensile properties of Inconel 718 fabricated by powder feeding laser additive manufacturing. *Acta Mater.* **2018**, *164*, 413–427. [CrossRef]
3. Deng, D. *Additively Manufactured Inconel 718: Microstructures and Mechanical Properties*; Linkoping University Electronic Press: Linkoping, Sweden, 2018; Volume 1798, p. 69.
4. Sun, W.; Bhowmik, A.; Tan, A.W.-Y.; Li, R.; Xue, F.; Marinescu, I.; Liu, E. Improving microstructural and mechanical characteristics of cold-sprayed Inconel 718 deposits via local induction heat treatment. *J. Alloys Compd.* **2019**, *797*, 1268–1279. [CrossRef]
5. Yin, S.; Cizek, J.; Cupera, J.; Hassani, M.; Luo, X.; Jenkins, R.; Xie, Y.; Li, W.; Lupoi, R. Formation conditions of vortex-like intermixing interfaces in cold spray. *Mater. Des.* **2021**, *200*, 109444. [CrossRef]
6. Assadi, H.; Kreye, H.; Gärtner, F.; Klassen, T. Cold spraying–A materials perspective. *Acta Mater.* **2016**, *116*, 382–407. [CrossRef]
7. Sun, W.; Tan, A.W.-Y.; Wu, K.; Yin, S.; Yang, X.; Marinescu, I.; Liu, E. Post-Process Treatments on Supersonic Cold Sprayed Coatings: A Review. *Coatings* **2020**, *10*, 123. [CrossRef]
8. Nault, I.M.; Ferguson, G.D.; Nardi, A.T. Multi-axis tool path optimization and deposition modeling for cold spray additive manufacturing. *Addit. Manuf.* **2021**, *38*, 101779. [CrossRef]
9. Wong, W.; Irissou, E.; Vo, P.; Sone, M.; Bernier, F.; Legoux, J.-G.; Fukanuma, H.; Yue, S. Cold Spray Forming of Inconel 718. *J. Therm. Spray Technol.* **2012**, *22*, 413–421. [CrossRef]
10. Pérez-Andrade, L.; Gärtner, F.; Villa-Vidaller, M.; Klassen, T.; Muñoz-Saldaña, J.; Alvarado-Orozco, J. Optimization of Inconel 718 thick deposits by cold spray processing and annealing. *Surf. Coat. Technol.* **2019**, *378*, 124997. [CrossRef]
11. Levasseur, D.; Yue, S.; Brochu, M. Pressureless sintering of cold sprayed Inconel 718 deposit. *Mater. Sci. Eng. A* **2012**, *556*, 343–350. [CrossRef]
12. Sun, W.; Tan, A.W.-Y.; Bhowmik, A.; Marinescu, I.; Song, X.; Zhai, W.; Li, F.; Liu, E. Deposition characteristics of cold sprayed Inconel 718 particles on Inconel 718 substrates with different surface conditions. *Mater. Sci. Eng. A* **2018**, *720*, 75–84. [CrossRef]
13. Sun, W.; Bhowmik, A.; Tan, A.W.-Y.; Xue, F.; Marinescu, I.; Li, F.; Liu, E. Strategy of incorporating Ni-based braze alloy in cold sprayed Inconel 718 coating. *Surf. Coat. Technol.* **2019**, *358*, 1006–1012. [CrossRef]

14. Sun, W.; Tan, A.W.-Y.; Bhowmik, A.; Xue, F.; Marinescu, I.; Liu, E. Evaluation of cold sprayed graphene nanoplates–Inconel 718 composite coatings. *Surf. Coat. Technol.* **2019**, *378*, 125065. [CrossRef]
15. Rahimi, S.; King, M.; Dumont, C. Stress relaxation behaviour in IN718 nickel based superalloy during ageing heat treatments. *Mater. Sci. Eng. A* **2017**, *708*, 563–573. [CrossRef]
16. Jinhui, D.; Xudong, L.; Qun, D.; Ying, L. Effect of Solution Treatment on the Microstructure and Mechanical Properties of IN718 Alloy. *Rare Met. Mater. Eng.* **2017**, *46*, 2359–2365. [CrossRef]
17. Entezarian, M.; Allaire, F.; Tsantrizos, P.; Drew, R.A.L. Plasma atomization: A new process for the production of fine, spherical powders. *JOM* **1996**, *48*, 53–55. [CrossRef]
18. Mostafa, A.; Picazo Rubio, I.; Brailovski, V.; Jahazi, M.; Medraj, M. Structure, Texture and Phases in 3D Printed IN718 Alloy Subjected to Homogenization and HIP Treatments. *Metals* **2017**, *7*, 196. [CrossRef]
19. Yan, S.; Wang, Y.; Wang, Q.; Zhang, C.; Chen, D.; Cui, G. Enhancing Mechanical Properties of the Spark Plasma Sintered Inconel 718 Alloy by Controlling the Nano-Scale Precipitations. *Materials* **2019**, *12*, 3336. [CrossRef]
20. Parimi, L.L.; Ravi, G.A.; Clark, D.; Attallah, M.M. Microstructural and texture development in direct laser fabricated IN718. *Mater. Charact.* **2014**, *89*, 102–111. [CrossRef]
21. Zhong, C.; Gasser, A.; Kittel, J.; Wissenbach, K.; Poprawe, R. Improvement of material performance of Inconel 718 formed by high deposition-rate laser metal deposition. *Mater. Des.* **2016**, *98*, 128–134. [CrossRef]
22. Sangid, M.D.; Book, T.A.; Naragani, D.; Rotella, J.; Ravi, P.; Finch, A.; Kenesei, P.; Park, J.-S.; Sharma, H.; Almer, J.; et al. Role of heat treatment and build orientation in the microstructure sensitive deformation characteristics of IN718 produced via SLM additive manufacturing. *Addit. Manuf.* **2018**, *22*, 479–496. [CrossRef]
23. Li, J.; Zhao, Z.; Bai, P.; Qu, H.; Liu, B.; Li, L.; Wu, L.; Guan, R.; Liu, H.; Guo, Z. Microstructural evolution and mechanical properties of IN718 alloy fabricated by selective laser melting following different heat treatments. *J. Alloys Compd.* **2019**, *772*, 861–870. [CrossRef]
24. Gao, Y.; Zhang, D.; Cao, M.; Chen, R.; Feng, Z.; Poprawe, R.; Schleifenbaum, J.H.; Ziegler, S. Effect of δ phase on high temperature mechanical performances of Inconel 718 fabricated with SLM process. *Mater. Sci. Eng. A* **2019**, *767*, 138327. [CrossRef]
25. Azadian, S.; Wei, L.-Y.; Warren, R. Delta phase precipitation in Inconel 718. *Mater. Charact.* **2004**, *53*, 7–16. [CrossRef]
26. Strondl, A.; Fischer, R.; Frommeyer, G.; Schneider, A. Investigations of MX and γ'/γ'' precipitates in the nickel-based superalloy 718 produced by electron beam melting. *Mater. Sci. Eng. A* **2008**, *480*, 138–147. [CrossRef]
27. Sun, W.; Tan, A.W.-Y.; King, D.J.Y.; Khun, N.W.; Bhowmik, A.; Marinescu, I.; Liu, E. Tribological behavior of cold sprayed Inconel 718 coatings at room and elevated temperatures. *Surf. Coat. Technol.* **2020**, . *385*, 125386. [CrossRef]
28. Sun, W.; Tan, A.W.-Y.; Khun, N.W.; Marinescu, I.; Liu, E. Effect of substrate surface condition on fatigue behavior of cold sprayed Ti6Al4V coatings. *Surf. Coat. Technol.* **2017**, *320*, 452–457. [CrossRef]
29. Lek, J.Y.; Bhowmik, A.; Tan, A.W.-Y.; Sun, W.; Song, X.; Zhai, W.; Buenconsejo, P.J.; Li, F.; Liu, E.; Lam, Y.M.; et al. Understanding the microstructural evolution of cold sprayed Ti-6Al-4V coatings on Ti-6Al-4V substrates. *Appl. Surf. Sci.* **2018**, *459*, 492–504. [CrossRef]
30. Song, X.; Jin, X.-Z.; Zhai, W.; Tan, A.W.-Y.; Sun, W.; Li, F.; Marinescu, I.; Liu, E. Correlation between the macroscopic adhesion strength of cold spray coating and the microscopic single-particle bonding behaviour: Simulation, experiment and prediction. *Appl. Surf. Sci.* **2021**, *547*, 149165. [CrossRef]
31. Wu, K.; Sun, W.; Tan, A.W.-Y.; Marinescu, I.; Liu, E.; Zhou, W. An investigation into microstructure, tribological and mechanical properties of cold sprayed Inconel 625 coatings. *Surf. Coat. Technol.* **2021**, *424*, 127660. [CrossRef]